

Cite this: DOI:00.0000/xxxxxxxxxx

Role of local structural distortions in the variation of martensitic transformation temperature with e/a ratio in $\text{Ni}_2\text{Mn}_{1+x}\text{Z}_{1-x}$ ($\text{Z} = \text{In, Sn or Sb}$) alloys [†]

Nafea Manea^a, Edmund Welter^b and K R Priolkar*^a

Received Date

Accepted Date

DOI:00.0000/xxxxxxxxxx

$\text{Ni}_2\text{Mn}_{1+x}\text{Z}_{1-x}$ ($\text{Z} = \text{In, Sn or Sb}$) undergo martensitic transformation with transformation temperature (T_M) scaling with the average valence electron per atom (e/a) ratio. However, the rate of increase of T_M depends on the type of Z atom, with the slope of T_M vs. e/a curve increasing from $\text{Z} = \text{In}$ to $\text{Z} = \text{Sb}$. Local structural distortions are believed to be the leading cause of martensitic transformation in these alloys. A careful study of the Ni and Mn local structures in several $\text{Ni}_2\text{Mn}_{1+x}\text{Z}_{1-x}$ alloys with varying e/a ratio and the same Z atom, with the same e/a ratio but different Z atoms and with the same T_M but with different Z atoms and different e/a ratio, revealed that the difference between Ni-Mn and Ni-Z nearest neighbor distances decreases as the Z atom changes from In to Sb. This decrease in the local structural distortion accommodates a higher content of Mn until the $L2_1$ structure becomes unstable and the alloy undergoes a martensitic transformation.

1 Introduction

In Heusler alloys, the average valence electron atom (e/a) ratio is a key parameter used to understand and predict the structural and electronic properties of these materials, particularly in relation to their magnetic behavior and potential applications in spintronics. The e/a ratio influences the electronic structure of a Heusler alloy, impacting its magnetic properties, stability, and potential applications. The ratio also significantly impacts the martensitic transformation temperature of the Heusler alloys and often a linear relationship between the martensitic transformation temperature and e/a is noted¹.

Ni_2MnZ ($\text{Z} = \text{In, Sn or Sb}$) are typical Heusler alloys that display a stable ferromagnetic $L2_1$ crystal structure even though their e/a ratio is equal to or larger than that of the famous ferromagnetic shape memory alloy, Ni_2MnGa . All three Ni-Mn-Z Heusler alloys display martensitic transition with an increase in their e/a ratio achieved by substituting the Z atoms with Mn, resulting in Mn-rich $\text{Ni}_2\text{Mn}_{1+x}\text{Z}_{1-x}$ alloys. Addition of Mn not only results in martensitic instability but also modifies the magnetic ground state and displays strong correlation between the structural and magnetic degrees of freedom. Such a strong interaction gives rise to a variety of effects such as the magnetic shape memory effect²⁻⁴, magnetic superelasticity⁵⁻⁹, the magnetocaloric effect^{10,11}, giant

magnetoresistance¹², exchange bias¹³, kinetic arrest^{14,15}, etc.

Structurally, these off-stoichiometric alloys transform from a high-temperature austenitic state with an $L2_1$ or $B2$ structure to a low-temperature martensitic state with either a low symmetry modulated structure or a tetragonal $L1_0$ structure depending on the amount of Mn replacing the Z atoms. The process of transformation usually occurs via one or more intermartensitic transformations, with the structure continuously evolving from one type of modulation to another¹⁶. In all the $\text{Ni}_2\text{Mn}_{1+x}\text{Z}_{1-x}$ ($\text{Z} = \text{In, Sn, Sb}$) alloys, the martensitic transformation appears at a particular value of Mn replacing the Z atoms (x), which is unique to the type of Z atom. The value of x increases with the Z atom changing from In to Sn to Sb. When $\text{Z} = \text{In}$, the critical value of $x \sim 0.35$ and increases to about 0.4 for $\text{Z} = \text{Sn}$ and to 0.45 for $\text{Z} = \text{Sb}$ ^{1,5}. The martensitic transformation temperature, T_M increases linearly with further substitution of Z atoms with Mn. Since a complete replacement of Z atoms by Mn results in the formation of binary NiMn alloy, the rate of increase of T_M as a function of e/a ratio also increases with a change in Z atom from In to Sb.

The magnetic ground state of these alloys also changes with the appearance of a martensitic transition. The stoichiometric compositions of these alloys are all ferromagnetic. Beyond the critical value of Mn atoms replacing the Z atoms, initially, the alloys transform from a ferromagnetic austenitic state to a magnetically complex martensitic state with competing ferromagnetic and antiferromagnetic interactions, often resulting in a glassy magnetic state. With further addition of Mn, the transformation occurs from paramagnetic austenitic state to antiferromagnetic state. The magnetic nature of these Ni-Mn-Z ($\text{Z} = \text{In, Sn and Sb}$) alloys is not well understood and needs to be studied in detail.

^a School of Physical and Applied Sciences, Goa University, Taleigao Plateau, Goa, India. Fax: 91 832 245184; Tel: 91 8669609210; E-mail: krp@unigoa.ac.in

^b Deutsches Elektronen-Synchrotron DESY, Notkestrasse 85, 22607 Hamburg, Germany

† Supplementary Information available: [details of any supplementary information available should be included here]. See DOI: 00.0000/00000000.

Sb) off-stoichiometric alloys has been very interesting and various explanations of the magnetic behavior of martensite have been proposed: paramagnetism, antiferromagnetism, superparamagnetism, re-entrant spin-glass, superspin glass, etc.^{1,4,17,18}.

Several studies have contemplated about the mechanism of martensitic transformation and the magnetic ground state of these alloys^{1,19,20}. Based on an empirical study of several Ni-Mn-Z (Z = Ga, In, Sn, Sb) Heusler alloys, it is suggested that martensitic transformation occurs in all alloy compositions with austenitic $L2_1$ unit cell lattice parameter $\leq 6 \text{ \AA}$ ²¹. Extended x-ray absorption fine structure studies probing the local structure around the constituent metal atoms in such $\text{Ni}_2\text{Mn}_{1+x}\text{Z}_{1-x}$ alloys have highlighted the role of the structural distortions in the nearest neighbor environment in inducing martensitic transformation²²⁻²⁴. The metastability of these Mn-rich alloys against thermal annealing, resulting in their phase separation into stoichiometric Heusler and tetragonal $L1_0$ phases²⁵, has further supported the role of local structural distortions in martensitic transformation. A random distribution of martensitic NiMn and ferromagnetic Heusler structural units results in the martensitic transformation at a critical value of x in $\text{Ni}_2\text{Mn}_{1+x}\text{Z}_{1-x}$ (Z = In, Sn, Sb) alloys²⁶. However, these studies do not explain the different critical values of x for different Z atoms. The critical x value in fact increases from In to Sb challenging the e/a rule. As a result, the slope of the T_M vs. e/a curves becomes steeper from Z = In to Z = Sb.

To understand the reasons for the dependence of T_M vs. e/a curve on the type of Z atom, eight different compositions with Z = In, Sn and Sb were studied. The compositions were chosen so that effect of the Z atom and e/a ratio could be compared and distinctly studied. We prepared four compositions with the same Z atom and varying e/a ratio, $\text{Ni}_2\text{Mn}_{1.3}\text{In}_{0.7}$ ($e/a = 7.8$), $\text{Ni}_2\text{Mn}_{1.35}\text{In}_{0.65}$ ($e/a = 7.85$), $\text{Ni}_2\text{Mn}_{1.4}\text{In}_{0.6}$ ($e/a = 7.9$) and $\text{Ni}_2\text{Mn}_{1.5}\text{In}_{0.5}$ ($e/a = 8.0$). While maintaining the e/a ratio = 8.0, the Z atom was varied from In ($\text{Ni}_2\text{Mn}_{1.5}\text{In}_{0.5}$) to Sn ($\text{Ni}_2\text{Mn}_{1.34}\text{Sn}_{0.66}$) to Sb (Ni_2MnSb). Three compositions with $T_M \approx 400\text{K}$ but different Z atoms and different e/a ratios were also studied. Here, the e/a ratio varied from 8.0 ($\text{Ni}_2\text{Mn}_{1.5}\text{In}_{0.5}$) to 8.2 ($\text{Ni}_2\text{Mn}_{1.6}\text{Sn}_{0.4}$) to 8.3 ($\text{Ni}_2\text{Mn}_{1.65}\text{Sb}_{0.35}$). Our studies confirmed the difference in the Mn-Z and Mn-Mn(Z) bond distances to be responsible for the martensitic transformation in these alloys.

2 Experimental

The polycrystalline $\text{Ni}_2\text{Mn}_{1+x}\text{Z}_{1-x}$ alloys were prepared by using an arc melting furnace. The correctly weighed amounts of the constituent elements (99.99% purity) were melted under an argon atmosphere in a water-cooled copper hearth. The ingots were flipped and melted four times to ensure the homogeneity of the samples. A low-speed diamond cutter was used to cut the samples into required pieces for different characterization techniques. The remaining part of the ingot was ground to a fine powder for structural characterization. These pieces and the powder were wrapped in a tantalum foil, encapsulated in an evacuated quartz tube, and annealed for 48 hours at 750 °C, followed by rapid quenching in ice cold water. The alloy compositions were checked

by Energy dispersive x-ray spectroscopy (SEM-EDS) on a Carl-Zeiss scanning electron microscope. X-ray diffraction (XRD) measurements were performed at room temperature in the 2θ range between 20 - 100 degrees using (Cu K_α) radiation on a Rigaku Smart Lab x-ray diffractometer. Magnetization M(T) measurements were carried out on Cryogenic S-700 SQUID magnetometer in the range of 5 K - 400 K. Samples were first cooled in zero applied magnetic field from room temperature to 5 K and the data was then recorded in 10 mT field while warming (ZFC), and subsequent cooling (FCC) and warming (FCW) cycles. Differential scanning calorimetry (DSC) measurements were carried out on Shimadzu DSC-60 in the temperature range 150 K - 600 K. Endothermic and exothermic heat output curves were recorded on each of the samples weighing about 4 mg - 5 mg, crimped in an aluminium pan and heated/ cooled at a constant rate of 5 K /minute.

X-ray absorption spectra were recorded at the Ni K (8333 eV) and Mn K (6539 eV) edges at room temperature at the P65 beamline at Petra III synchrotron source, DESY, Hamburg, Germany, using Si(111) double crystal monochromator and two Si mirrors at an angle of incidence of 2 mrad for higher harmonics suppression, a standard configuration for this energy range²⁷. The two crystals were detuned to 90% of maximum intensity to further suppress the higher order harmonics. The incident (I_0) and the transmitted (I) photon intensities were simultaneously measured using gas ionization chambers with appropriate gases.

The absorbers were prepared by coating scotch tape with extremely fine alloy powder. The thickness of the absorber was adjusted by changing the number of layers of scotch tape to obtain a total absorption, $\mu t \leq 2.5$ above the edge. The data was treated as per standard procedure in Demeter suite²⁸.

3 Results

The compositions of all the $\text{Ni}_2\text{Mn}_{1+x}\text{Z}_{1-x}$ alloys were determined from SEM-EDS by averaging the elemental content over a $100 \mu\text{m}^2$ area of the sample. These results are tabulated in Table 1. The obtained alloy compositions were found to be close to the nominal compositions and were used to determine the e/a ratio of the alloys. Along with the nominal and obtained compositions of the alloys, Table 1 also lists the e/a ratio, structure of the alloys at room temperature ($\sim 300\text{K}$) determined from the Le Bail refinement of the XRD patterns and the martensitic transformation temperature (T_M). The presence of a martensitic transformation in all the alloys was checked by DSC and magnetization measurements. Heat output curves obtained from the DSC measurements are given in the Figure S1 in the Supporting Information and the magnetization measurements are discussed below.

The alloy compositions in the present study were chosen to satisfy three conditions; (a) Varying e/a ratio but same Z atom – $\text{Ni}_2\text{Mn}_{1.3}\text{In}_{0.7}$, $\text{Ni}_2\text{Mn}_{1.35}\text{In}_{0.65}$, $\text{Ni}_2\text{Mn}_{1.4}\text{In}_{0.6}$ and $\text{Ni}_2\text{Mn}_{1.5}\text{In}_{0.5}$; (b) Varying Z atom but same e/a ratio – $\text{Ni}_2\text{Mn}_{1.5}\text{In}_{0.5}$, $\text{Ni}_2\text{Mn}_{1.33}\text{Sn}_{0.67}$ and Ni_2MnSb and (c) Varying Z atom and varying e/a ratio but same martensitic transformation temperature, T_M – $\text{Ni}_2\text{Mn}_{1.5}\text{In}_{0.5}$, $\text{Ni}_2\text{Mn}_{1.6}\text{Sn}_{0.4}$ and $\text{Ni}_2\text{Mn}_{1.65}\text{Sb}_{0.35}$.

The XRD patterns for all eight alloys recorded at room temperature (RT) are shown in Figs. 1 and 2. All the compounds are

Table 1 SEM-EDS composition, e/a ratio, room temperature structure and T_M of the $\text{Ni}_2\text{Mn}_{1+x}\text{Z}_{1-x}$ ($\text{Z} = \text{In}, \text{Sn}, \text{Sb}$) alloys

Alloy	EDAX composition	e/a	Structure	T_M (K)
$\text{Ni}_2\text{Mn}_{1.3}\text{In}_{0.7}$	$\text{Ni}_{1.99}\text{Mn}_{1.26}\text{In}_{0.75}$	7.74	cubic	—
$\text{Ni}_2\text{Mn}_{1.35}\text{In}_{0.65}$	$\text{Ni}_{2.02}\text{Mn}_{1.34}\text{In}_{0.64}$	7.88	cubic	200
$\text{Ni}_2\text{Mn}_{1.4}\text{In}_{0.6}$	$\text{Ni}_{2.04}\text{Mn}_{1.36}\text{In}_{0.60}$	7.93	7M	335
$\text{Ni}_2\text{Mn}_{1.5}\text{In}_{0.5}$	$\text{Ni}_{2.08}\text{Mn}_{1.46}\text{In}_{0.46}$	8.10	7M	436
$\text{Ni}_2\text{Mn}_{1.33}\text{Sn}_{0.67}$	$\text{Ni}_{2.03}\text{Mn}_{1.32}\text{Sn}_{0.65}$	8.03	cubic	—
Ni_2MnSb	$\text{Ni}_{2.06}\text{Mn}_{1.01}\text{Sb}_{0.93}$	8.08	cubic	—
$\text{Ni}_2\text{Mn}_{1.6}\text{Sn}_{0.4}$	$\text{Ni}_{2.07}\text{Mn}_{1.56}\text{Sn}_{0.37}$	8.26	7M	434
$\text{Ni}_2\text{Mn}_{1.65}\text{Sb}_{0.35}$	$\text{Ni}_{2.05}\text{Mn}_{1.68}\text{Sb}_{0.27}$	8.40	7M & 4O	439

single phase with no noticeable impurity phases. The lattice parameters of the alloys computed by Rietveld refinement are given in the Table S1 in the Supporting Information. The alloys are then classified into three groups mentioned above and their diffraction patterns over a limited angular range are compare in the Fig. 3. First group represents alloys with varying e/a ratio and same Z atom ($\text{Z} = \text{In}$) (Fig. 3(a)). Here the room temperature structure of the alloys changes from cubic $L2_1$ to incommensurately modulated 7M with increasing e/a ratio. Such a change in the crystal structure indicates an increase in the martensitic transformation temperature with e/a ratio. It should be noted, however, in the case of Ni-Mn-In alloys, martensitic transformation is noted in alloys with $e/a \geq 7.85^{24}$.

A comparison RT XRD of alloys with similar e/a ratio (~ 8.1) but with different Z atoms ($\text{Z} = \text{In}, \text{Sn}$ and Sb) (Fig. 3(b)) shows that only the Ni-Mn-In alloy has a modulated structure at RT. The other two alloys, $\text{Ni}_2\text{Mn}_{1.33}\text{Sn}_{0.67}$ and Ni_2MnSb display a cubic structure which implies a possible martensitic transformation below RT or no transformation at all. The critical values of e/a ratio at which martensitic transformation occurs in $\text{Ni}_2\text{Mn}_{1+x}\text{Sn}_{1-x}$ and $\text{Ni}_2\text{Mn}_{1+x}\text{Sb}_{1-x}$ alloys are respectively reported as 8.15 and 8.20^{1,5}. Hence it is likely that $\text{Ni}_2\text{Mn}_{1.33}\text{Sn}_{0.67}$ and Ni_2MnSb do not undergo martensitic transformation even below room temperature.

In the third category of alloys, both, the e/a ratio and Z atom are varied to ensure that the alloys transform at $T_M \sim 400$ K (Fig. 3(c)). Here the least e/a ratio ($e/a = 8.10$) is observed for the alloy with $\text{Z} = \text{In}$ and highest ($e/a = 8.40$) for $\text{Z} = \text{Sb}$. Further, incommensurately 7M modulated crystal structures are obtained for alloys with $\text{Z} = \text{In}$ and Sn and a mixture of 7M and 4O structure is noted in case of $\text{Ni}_2\text{Mn}_{1.65}\text{Sb}_{0.35}$.

Thus it can be seen that for a given value of e/a ratio (8.10 in the present case), alloys realized with different Z atoms do not undergo martensitic transformation at the same temperature. Similarly, if a demand is made that martensitic transformation temperature remains the same irrespective of Z atom, the e/a ratio increases from $\text{Z} = \text{In}$ to Sb . Considering the end member composition achieved after a complete replacement of Z atom, is NiMn in all the three cases, the above variation of crystal structure at room temperature and the relative concentration of the Z atom for In, Sn and Sb clearly indicate that the critical value of e/a ratio at which the alloys display martensitic instability and the slope of T_M vs. e/a curve increases from $\text{Z} = \text{In}$ to $\text{Z} = \text{Sb}$.

Magnetization as a function of temperature M(T) recorded in 5 K $\leq T \leq 390$ K in an applied field of 100 Oe during the ZFC, FCC

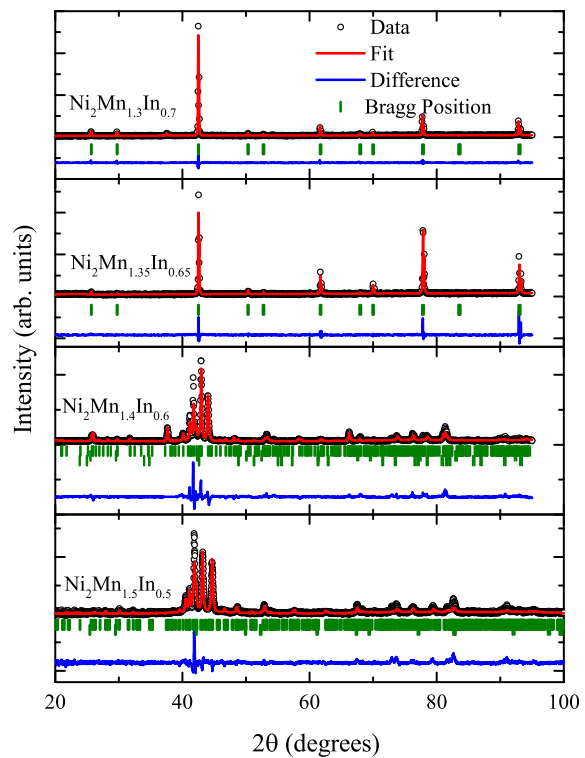


Fig. 1 Rietveld refined X-ray diffraction patterns of $\text{Ni}_2\text{Mn}_{1+x}\text{In}_{1-x}$, $x = 0.3, 0.35, 0.4$ and 0.5 recorded at room temperature.

and FCW cycles for all the eight alloy compositions studied here is presented in Fig. 4. Of the eight alloys, four alloys, $\text{Ni}_2\text{Mn}_{1.3}\text{In}_{0.7}$, $\text{Ni}_2\text{Mn}_{1.35}\text{In}_{0.65}$, $\text{Ni}_2\text{Mn}_{1.34}\text{Sn}_{0.66}$ and $\text{Ni}_2\text{Mn}_{1.06}\text{Sb}_{0.94}$ display a ferromagnetic order with transition temperature T_C , respectively, equal to 307 K, 305 K, 325 K and 347 K. Whereas the other four alloys have a very low value of magnetization at 5 K in their ZFC state and large bifurcation between ZFC and FC magnetization curves indicating a complex magnetic order due to competing antiferromagnetic interactions. The antiferromagnetic interactions are believed to arise from an indirect interaction between the Mn atoms in its own, Y sub-lattice and those in the Z sub-lattice of the X_2YZ Heusler structure²⁹. However, both, theory and experiments have also indicated other exchange mechanisms to be responsible for the antiferromagnetic interactions^{30,31}. The proposed exchange mechanism mainly arise due to presence of local structural distortions present in such non-stoichiometric Ni-Mn-Z Heusler alloys^{23,30}.

The left panel of Fig. 4 displays M(T) behavior of the four Ni-Mn-In alloys. Martensitic transformation first appears just below 200 K in $\text{Ni}_2\text{Mn}_{1.35}\text{In}_{0.65}$ ($e/a = 7.88$) in its ferromagnetic state ($T_C = 305$ K). $\text{Ni}_2\text{Mn}_{1.3}\text{In}_{0.7}$ ($e/a = 7.74$) does not display any martensitic transformation down to the lowest measured temperature. With further increase in the e/a ratio, the martensitic trans-

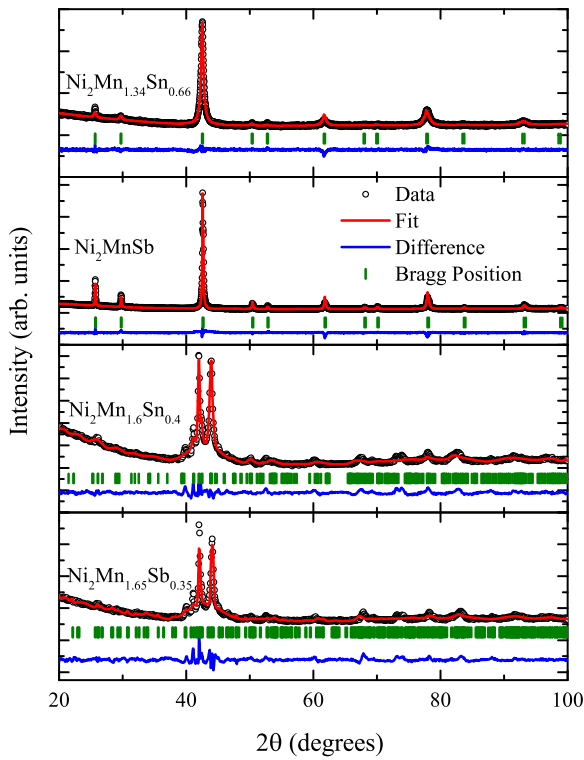


Fig. 2 Rietveld refined X-ray diffraction patterns of $\text{Ni}_2\text{Mn}_{1.34}\text{Sn}_{0.66}$, Ni_2MnSb , $\text{Ni}_2\text{Mn}_{1.6}\text{Sn}_{0.4}$ and $\text{Ni}_2\text{Mn}_{1.65}\text{Sn}_{0.35}$ recorded at room temperature.

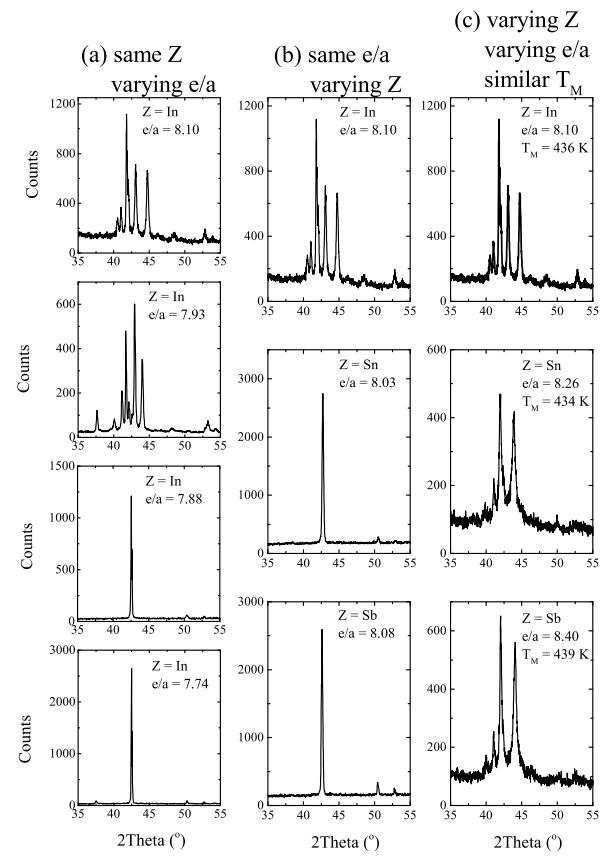


Fig. 3 X-ray diffraction patterns of $\text{Ni}_2\text{Mn}_{1+x}\text{Z}_{1-x}$ ($\text{Z} = \text{In}$, Sn and Sb) alloys recorded at room temperature. For the sake of understanding, the diffraction patterns are arranged as per the e/a ratio of the alloys.

formation temperature continuously increases from 200 K to 420 K in $\text{Ni}_2\text{Mn}_{1.5}\text{In}_{0.5}$ ($e/a = 8.10$). For $\text{Ni}_2\text{Mn}_{1.4}\text{In}_{0.6}$ ($T_M = 330$ K (indicated by an arrow in Fig.4)) and $\text{Ni}_2\text{Mn}_{1.5}\text{In}_{0.5}$ alloys, the martensitic transformation occurs in the paramagnetic state.

A comparison of alloys with similar e/a ratio ≈ 8.0 but different Z atoms, reveals that alloys with $\text{Z} = \text{Sn}$ and In do not undergo martensitic transformation down to 5 K. To achieve a T_M similar to that of $\text{Ni}_2\text{Mn}_{1.5}\text{In}_{0.5}$ ($e/a = 8.10$) with $\text{Z} = \text{Sn}$ and Sb , one needs to increase the e/a ratio to 8.26 and 8.35 respectively. This magnetization behavior corroborates the earlier conclusion of critical value of e/a ratio to induce martensitic transformation and a higher slope of T_M vs. e/a curve for $\text{Z} = \text{Sn}$ and Sb .

To understand the cause for different T_M vs. e/a curve slopes for $\text{Z} = \text{In}$ Sn and Sb , local structures around Mn and Ni atoms were investigated using EXAFS in all eight alloys. The k^2 -weighted EXAFS data, $\chi(k)$ extracted from Mn and Ni K absorption data are presented in the Figure S2 and S3 in the Supporting Information. Fine structure oscillations can be clearly observed up to $k = 14 \text{ \AA}^{-1}$. Previous EXAFS studies on such alloys have indicated a presence of local structural disorder in the near neighbor environment of Mn and Ni²²⁻²⁴. In particular, the nearest neighbor Ni-Mn distance is always shorter than Ni-Z dis-

tance in all non-stoichiometric Ni-Mn-Z alloys despite the requirement of them being equal by the $L2_1$ symmetry. This disorder is present even in alloy compositions that do not undergo a martensitic transformation. It has been believed that these structural distortions promote a Ni_{3d} - Mn_{3d} hybridization that facilitates martensitic transformation^{22,30,32}.

The Fourier transform magnitudes of the Mn K, and Ni K edge EXAFS recorded at RT in the four $\text{Ni}_2\text{Mn}_{1+x}\text{In}_{1-x}$ alloys are presented in Fig. 5. Fig. 6 gives the magnitudes of Fourier transform of Mn and Ni EXAFS in the $\text{Ni}_2\text{Mn}_{1+x}\text{Sn}_{1-x}$ and $\text{Ni}_2\text{Mn}_{1+x}\text{Sb}_{1-x}$ alloys. The experimental data was fitted to a structural model constructed based on the crystal structure of the alloys. Both Mn and Ni EXAFS were fitted together in one fit with the common set of variable parameters. The varied parameters are tabulated in the supplementary information. The k-space EXAFS data in the range for 3 to 14 \AA^{-1} were used for fitting. The fits were performed in the R-space from 1 to 4 \AA for Mn EXAFS and from 1 to 3 \AA for Ni EXAFS data. Amplitude reduction factor (S_0^2) for Ni and Mn were estimated from the respective metal foils and kept fixed throughout the analysis. The values of S_0^2 used were 0.7 and 0.8 for Mn and Ni respectively. The best fit to the data is pre-

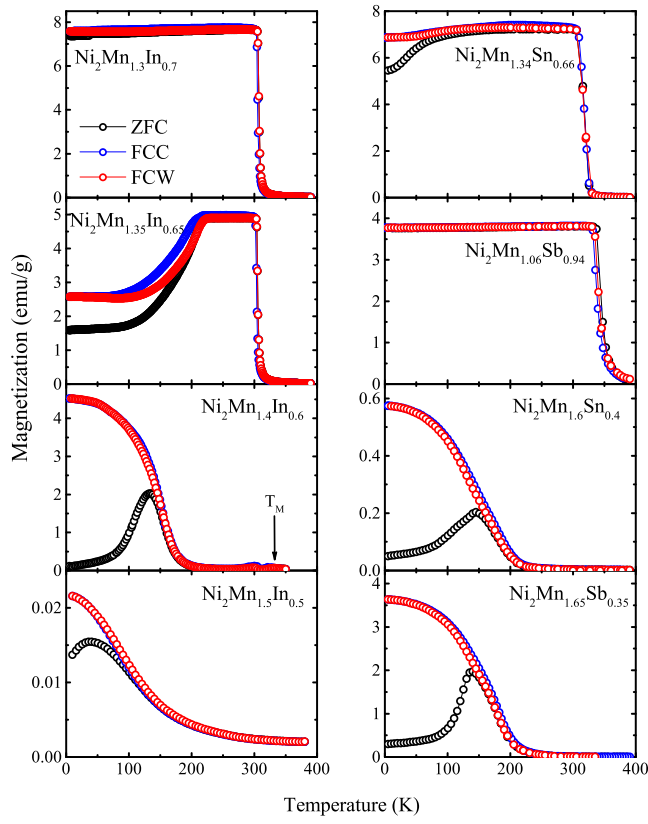


Fig. 4 Magnetization as a function of temperature measured in a temperature interval of 5 K – 390 K in a field of 100 Oe during ZFC, FCC and FCW cycles.

sented as a continuous line in both figs. 5 and 6. The obtained structural parameters are listed in Table 2.

A comparison of bond distances indicates that irrespective of the Z atom and the ground state of the alloy, the nearest neighbor Ni-Mn bond distance, is shorter than the Ni-Z bond distance. Further, the second neighbor Mn-Z and Mn-Mn_Z bond distances are nearly equal in all austenitic alloys, while in alloys that are martensitic at RT, the Mn-Mn_Z distance is greater than Mn-Z distance. Finally, the third nearest neighbor Mn-Mn bond distance is about 4.2 Å in ferromagnetic alloys while it increases to 4.3 Å in alloys with dominant antiferromagnetic interactions. These observations agree with earlier studies on Ni₂Mn_{1+x}In_{1-x} alloys^{23,24,33} and Ni₂Mn_{1.4}Sn_{0.6}²².

4 Discussion

Substitution of Mn at the Z atom sites in Ni₂MnZ (Z = In, Sn or Sb) or conversely replacing Mn by Z atoms in the binary Ni₅₀Mn₅₀ has a significant effect on the martensitic as well as magnetic ground states of these alloys. There have been several experimental and theoretical studies on the evolution of structure, magnetic and martensitic properties that have paved way for design of better alloys for several applications^{16,34-37}. However, a detailed

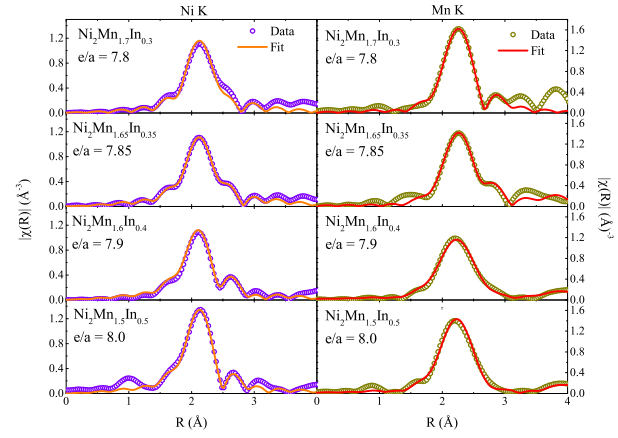


Fig. 5 Fourier transform magnitudes of the Ni K and Mn K edge EXAFS data in the four Ni-Mn-In alloys recorded at room temperature. The continuous line denotes the best fit to the data.

analysis on the role of different Z atoms in inducing these properties are missing.

It has been argued in the literature that the Heusler structure of Ni₂Mn_{1+x}Z_{1-x} can accommodate the strain caused by the size difference between the Z atom and Mn. The strain accommodation is up to a critical doping content beyond which the non-stoichiometric alloy undergoes a martensitic transformation. The structural strain due to size difference between the Mn and Z atoms can be estimated by the difference in Mn-Z and Mn-Mn_Z bond distances. Fig. 7 shows a plot of difference between Mn-Mn_Z and Mn-Z bond distance as a function of the *e/a* ratio. In the case of austenitic alloys, irrespective of the Z atom, the difference between the two bond distances is nearly zero. On the other hand, a difference of ~ 10% between Mn-Mn_Z and Mn-Z bond distances is noted for the martensitic alloys, and it increases further with increasing *e/a* ratio of the alloys.

Another intriguing aspect of these Mn-rich alloys is that they undergo a phase separation into a Heusler and a L1₀ phase upon temper annealing^{25,38,39}. The shorter Ni-Mn bond distance could result from the segregation of NiMn type structural entities in these Mn-rich alloys²⁶. Fig. 8 compares Ni-Mn and Ni-Z bond distances as a function of the *e/a* ratio for the alloys with different Z atoms. Regardless of the type of Z atom, the Ni-Mn bond distance seems to decrease linearly with increasing *e/a* ratio. In contrast, the Ni-Z bond distance displays a completely different behavior. Although their specific trends remain unclear, the Ni-In bond distances are larger than the Ni-Sn which are larger than Ni-Sb bond lengths.

The behavior of the nearest neighbor distances reveals the reason for the higher critical values of *e/a* at which martensitic transformation occurs in Ni₂Mn_{1+x}Sn_{1-x} and Ni₂Mn_{1+x}Sb_{1-x}. Fig. 8 shows that the difference between Ni-Mn and Ni-Z bond distances progressively decrease as Z changes from In to Sn to Sb. Ideally, in L2₁ symmetry, the two nearest neighbor bond distances, Ni-Mn

Table 2 Bond length (R) and mean square radial disorder (σ^2) of the near neighbor correlations around Mn and Ni in $\text{Ni}_2\text{Mn}_{1+x}\text{Z}_{1-x}$ (Z = In, Sn, Sb) alloys

Alloy	Bonds									
	Ni-Mn		Ni-Z		Mn-Z	Mn-Mn _Z	Mn-Mn			
R Å	$\sigma^2 \text{ Å}^2$	R Å	$\sigma^2 \text{ Å}^2$	R Å	$\sigma^2 \text{ Å}^2$	R Å	$\sigma^2 \text{ Å}^2$	R Å	$\sigma^2 \text{ Å}^2$	
$\text{Ni}_2\text{Mn}_{1.3}\text{In}_{0.7}$	2.589(10)	0.010(1)	2.627(10)	0.006(1)	2.930(20)	0.005(2)	2.935(20)	0.005(2)	4.254(20)	0.015(2)
$\text{Ni}_2\text{Mn}_{1.35}\text{In}_{0.65}$	2.585(6)	0.013(1)	2.640(6)	0.005(1)	2.916(20)	0.003(2)	2.941(10)	0.006(3)	4.245(30)	0.016(2)
$\text{Ni}_2\text{Mn}_{1.4}\text{In}_{0.6}$	2.582(8)	0.012(1)	2.625(10)	0.006(1)	2.894(61)	0.043(14)	2.981(26)	0.022(8)	4.341(35)	0.025(3)
$\text{Ni}_2\text{Mn}_{1.5}\text{In}_{0.5}$	2.571(8)	0.009(1)	2.620(8)	0.004(1)	2.880(100)	0.035(15)	2.999(80)	0.021(7)	4.341(35)	0.028(3)
$\text{Ni}_2\text{Mn}_{1.33}\text{Sn}_{0.67}$	2.572(4)	0.010(1)	2.603(4)	0.006(1)	2.940(20)	0.008(1)	2.950(10)	0.007(2)	4.210(20)	0.013(2)
Ni_2MnSb	2.567(3)	0.010(1)	2.585(3)	0.008(1)	2.959(17)	0.013(2)	2.959(17)	0.013(2)	4.233(20)	0.012(2)
$\text{Ni}_2\text{Mn}_{1.6}\text{Sn}_{0.4}$	2.572(7)	0.010(1)	2.593(5)	0.005(1)	2.890(100)	0.032(16)	3.070(40)	0.023(6)	4.330(40)	0.024(3)
$\text{Ni}_2\text{Mn}_{1.65}\text{Sb}_{0.35}$	2.561(6)	0.010(1)	2.591(9)	0.007(1)	2.870(70)	0.029(10)	3.040(30)	0.023(4)	4.310(40)	0.025(3)

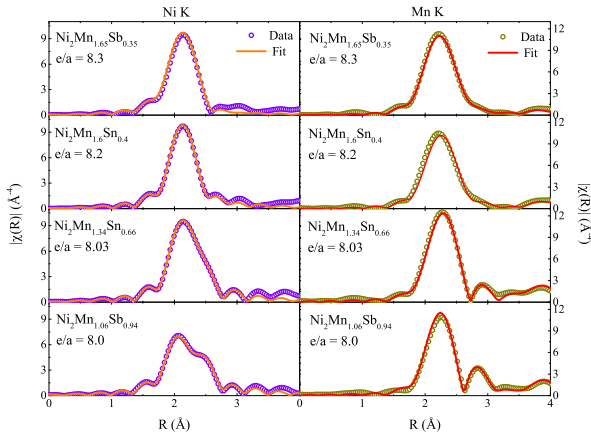


Fig. 6 Magnitude of Fourier transforms of EXAFS (open circles) along with the best fits (line) at the Ni and Mn K edges in Ni-Mn-Sn and Ni-Mn-Sb alloys.

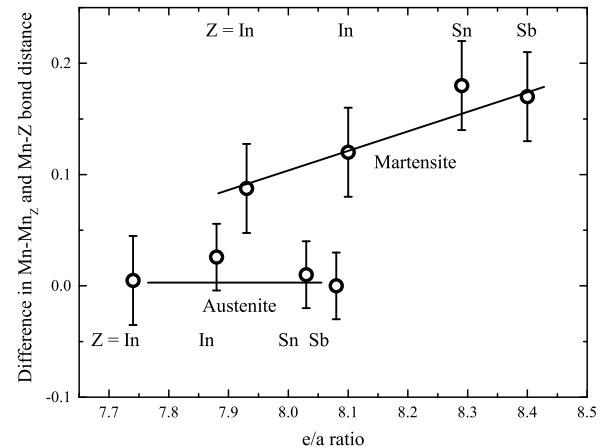


Fig. 7 Difference in the second nearest neighbor Mn-Z and Mn-Mn_Z as a function of e/a ratio in the Ni-Mn-Z alloys. The solid lines are only a guide to the eye.

and Ni-Z, should be equal. However, disparities are seen between these two bond distances in the cubic and martensitic phases of such Mn-rich alloys.

Replacement of Z atoms by Mn also segregates NiMn type structural units in a Heusler matrix³⁸. The nearest neighbor Ni-Mn bond distance in the *B2* or *L1₀* phase of NiMn is shorter than the Ni-Mn bond distance in the Heusler phase, producing a local strain. It has been recently shown that this strain drives the martensitic instability in Ni-Mn-In alloys²⁶. Therefore, the difference between Ni-Mn and Ni-Z bond distances in $\text{Ni}_2\text{Mn}_{1+x}\text{Z}_{1-x}$ alloys indicates presence of local strain produced by the replacement of the Z atom by Mn in these alloys. A smaller difference between the two distances implies lower strain or better compatibility between NiMn and Ni_2MnZ structural units which are formed locally in these off-stoichiometric alloys. A lower strain will also accommodate a larger amount of Mn at the Z atom site before the structure transforms from the cubic structure to a lower symmetry martensitic structure. Therefore, the critical concentration of Mn at which martensitic transformation occurs, progressively increases from In to Sn to Sb. Since the end member achieved after a complete replacement of Z atom is NiMn for all the three Z members considered here, the slope of variation of

T_M vs. e/a ratio also progressively increases from In to Sb. The locally segregated NiMn type structural units also affect the magnetic ground state of these alloys. Presence of antiferromagnetic NiMn structural units weaken the long range ferromagnetic interactions leading to disappearance of austenitic T_C . Increasing Mn content leads to the growth of antiferromagnetic clusters and shrinking of ferromagnetic Ni_2MnZ type ferromagnetic clusters. The strong competition between these ferromagnetic and antiferromagnetic clusters gives rise to a spin glass state. This is aptly clear from the similarities of the magnetization behaviour of all Ni-Mn-Z alloys with same T_M in Fig. 4.

Conclusions

In summary, several $\text{Ni}_2\text{Mn}_{1+x}\text{Z}_{1-x}$ (Z = In, Sn and Sb) alloys were investigated to understand the cause of different slopes of T_M vs. e/a curves for different Z atoms. In the case of alloys with the same Z atom and increasing e/a ratio, the difference between the nearest neighbor Ni-Mn and Ni-Z bond distances remains nearly constant irrespective of the state of the alloy. A distortion in the second nearest neighbor distances, Mn-Z and Mn-Mn_Z appears in the martensitic alloys. Such first and second neighbor distortion cause a strain to develop in the *L2₁* structure

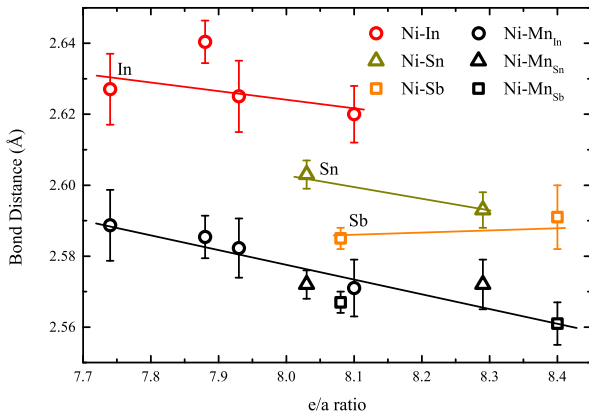


Fig. 8 Variation of the nearest neighbor Ni-Mn and Ni-Z bond distances in the Ni-Mn-Z alloys as a function of e/a ratio. The solid lines are only a guide to the eye.

due to the different atomic sizes of Mn and Z atoms. This strain is accommodated up to a critical concentration of Mn, and beyond which the alloy transforms martensitically to a lower symmetry structure.

A change in the Z atom from In to Sn and Sb in $\text{Ni}_2\text{Mn}_{1+x}\text{Z}_{1-x}$ while keeping their e/a ratio similar shows that the critical value of x at which the martensitic transformation appears depends on the type of Z atom. In the present case, the alloys with $Z = \text{Sn}$ and Sb with $e/a \sim 8$ are ferromagnetic austenitic down to the lowest temperature investigated. Martensitic transformation at the same temperature as $\text{Ni}_2\text{Mn}_{1.5}\text{In}_{0.5}$ ($e/a \sim 8$) can be achieved in alloys with $Z = \text{Sn}$ and Sb at an e/a ratio of 8.3 and 8.4, respectively. While the second neighbor distortions appear only in the martensitic compositions of Ni-Mn-Sn and Ni-Mn-Sb alloys, the nearest neighbor distortion decreases progressively from $Z = \text{In}$ to Sn to Sb. The lower first neighbor distortion or lower strain allows for accommodation of higher content of Mn at the Z atom site as the Z atom changes from In to Sb, and hence the martensitic transformation appears at a higher value of Mn content. Since the end member alloy in all three cases is NiMn, the increasingly higher values of Mn content at the Z atom site implies a steeper slope for the T_M vs. e/a ratio curves as the Z atoms change from In to Sn to Sb.

Author contributions

Nafea Manea: Data curation, Formal analysis, Methodology, Investigation, Validation, Visualization and Writing - Original draft. Edmund Welter: Data Curation, Investigation, Resources and Writing - review and editing. K. R. Priolkar: Conceptualization, Data curation, Formal analysis, Methodology, Fund acquisition, Resources, Validation, Visualisation and Writing - review and editing.

Conflicts of interest

There are no conflicts to declare.

Data availability

The data supporting this article have been included as part of the Supplementary Information.

Acknowledgements

KRP thanks Council of Scientific and Industrial Research, New Delhi for financial assistance under 03/1481/2023/EMR-II. We acknowledge DESY (Hamburg, Germany), a member of the Helmholtz Association HGF, for the provision of experimental facilities. Parts of this research were carried out at Petra III using P65 beamline. Beamtime was allocated for proposal I-20210145. Support from the Department of Science and Technology, Govt. of India within the framework of India DESY collaboration is acknowledged. Anuradha Bhogra is thanked for her assistance in EXAFS measurements. Facilities at the University Laboratory for Materials Characterization, Goa University are also gratefully acknowledged. Assistance of Elaine Dias and Bholanath Pahari is acknowledged in magnetization measurements.

Notes and references

- 1 A. Planes, L. Mañosa and M. Acet, *J.Phys.: Condens Matter*, 2009, **21**, 233201.
- 2 V. A. Chernenko, E. Cesari, V. V. Kokorin and I. N. Vitenko, *Scripta Metal. Mater.*, 1995, **33**, 1239.
- 3 K. Ullakko, J. K. Huang, C. Kantner, R. C. O'Handley and V. V. Kokorin, *Appl. Phys. Lett.*, 1996, **69**, 1966.
- 4 R. Y. Umetsu, R. Kainuma, Y. Amako, Y. Taniguchi, T. Kanomata, K. Fukushima, A. Fujita, K. Oikawa and K. Ishida, *Applied Physics Letters*, 2008, **93**, 042509.
- 5 Y. Sutou, Y. Imano, N. Koeda, T. Omori, R. Kainuma, K. Ishida and K. Oikawa, *Appl. Phys. Lett.*, 2004, **85**, 4358.
- 6 T. Krenke, M. Acet, E. F. Wassermann, X. Moya, L. Mañosa and A. Planes, *Phys. Rev. B*, 2005, **72**, 014412.
- 7 T. Krenke, M. Acet, E. F. Wassermann, X. Moya, L. Mañosa and A. Planes, *Phys. Rev. B*, 2006, **73**, 174413.
- 8 T. Krenke, E. Duman, M. Acet, E. F. Wassermann, X. Moya, L. Mañosa, A. Planes, E. Suard and B. Ouladdiaf, *Phys. Rev. B*, 2007, **75**, 104414.
- 9 R. Kainuma, Y. Imano, W. Ito, Y. Sutou, H. Morito, S. Okamoto, O. Kitakami, K. Oikawa, A. Fujita, T. Kanomata and K. Ishida, *Nature*, 2006, **439**, 957.
- 10 T. Krenke, E. Duman, M. Acet, E. F. Wassermann, X. Moya, L. Mañosa and A. Planes, *Nat. Mater.*, 2005, **4**, 450.
- 11 X. Moya, L. Mañosa, A. Planes, S. Aksoy, M. Acet, E. F. Wassermann and T. Krenke, *Phys. Rev. B*, 2007, **75**, 184412.
- 12 S. Chatterjee, S. Giri, S. Majumdar and S. K. De, *J. Phys. D Appl. Phys.*, 2009, **42**, 065001.
- 13 M. Khan, I. Dubenko, S. Stadler and N. Ali, *Appl. Phys. Lett.*, 2007, **91**, 072510.
- 14 W. Ito, K. Ito, R. Y. Umetsu, R. Kainuma, K. Koyama, K. Watanabe, A. Fujita, K. Oikawa, K. Ishida and T. Kanomata, *Appl. Phys. Lett.*, 2008, **92**, 021908.
- 15 V. K. Sharma, M. K. Chattopadhyay and S. B. Roy, *Phys. Rev. B*, 2007, **76**, 140401(R).

16 A. Çakır, L. Righi, F. Albertini, M. Acet and M. Farle, *Acta Materialia*, 2015, **99**, 140–149.

17 V. V. Khovaylo, T. Kanomata, T. Tanaka, M. Nakashima, Y. Amako, R. Kainuma, R. Y. Umetsu, H. Morito and H. Miki, *Phys. Rev. B*, 2009, **80**, 144409.

18 S. Chatterjee, S. Giri, S. K. De and S. Majumdar, *Phys. Rev. B*, 2009, **79**, 092410.

19 P. Entel, V. Buchelnikov, V. Khovailo, A. Zayak, W. Adeagbo, M. Gruner, H. Herper and E. Wassermann, *Journal of Physics D: Applied Physics*, 2006, **39**, 865 – 889.

20 V. D. Buchelnikov, V. V. Sokolovskiy, S. V. Taskaev, V. V. Khovaylo, A. A. Aliev, L. N. Khanov, A. B. Batdalov, P. Entel, H. Miki and T. Takagi, *Journal of Physics D: Applied Physics*, 2011, **44**, 064012.

21 T. Krenke, *PhD Thesis Universitat Duisburg-Essen, Duisburg*, 2007.

22 P. Bhobe, K. Priolkar and P. Sarode, *Journal of Physics: Condensed Matter*, 2007, **20**, 015219.

23 D. N. Lobo, K. R. Priolkar, P. A. Bhobe, D. Krishnamurthy and S. Emura, *Appl. Phys. Lett.*, 2010, **96**, 38006.

24 R. Nevgi, K. R. Priolkar, L. Righi, M. Solzi, F. Cugini, E. T. Dias and A. K. Nigam, *J.Phys.: Condens. Matter*, 2020, **32**, 505801.

25 L. Dincklage, F. Scheibel, A. Çakır, M. Farle and M. Acet, *AIP Advances*, 2018, **8**, year.

26 R. Nevgi, E. T. Dias and K. R. Priolkar, *Phys. Rev. B*, 2021, **104**, 054101.

27 E. Welter, R. Chernikov, M. Herrmann and R. Nemausat, *AIP Conference Proceedings*, 2019, **2054**, 040002.

28 B. Ravel and M. Newville, *J Synchrotron Radiat*, 2005, **12**, 537.

29 V. D. Buchelnikov, P. Entel, S. V. Taskaev, V. V. Sokolovskiy, A. Hucht, M. Ogura, H. Akai, M. E. Gruner and S. K. Nayak, *Phys. Rev. B*, 2008, **78**, 184427.

30 K. R. Priolkar, P. A. Bhobe, D. N. Lobo, S. W. D’Souza, S. R. Barman, A. Chakrabarti and S. Emura, *Phys. Rev. B*, 2013, **87**, 144412.

31 E. Şaşioğlu, L. M. Sandratskii and P. Bruno, *Phys. Rev. B*, 2008, **77**, 064417.

32 M. Ye, A. Kimura, Y. Miura, M. Shirai, Y. T. Cui, K. Shimada, H. Namatame, M. Taniguchi, S. Ueda, K. Kobayashi, R. Kainuma, T. Shishido, K. Fukushima and T. Kanomata, *Phys. Rev. Lett.*, 2010, **104**, 176401.

33 P. A. Bhobe, K. R. Priolkar and S. P. R., *J. Phys. D: Appl. Phys*, 2008, **41**, 045004.

34 A. G. Varzaneh, P. Kameli, I. A. Sarsari, M. G. Zavareh, C. S. Mejía, T. Amiri, Y. Skourski, J. L. Luo, T. H. Etsell and V. A. Chernenko, *Phys. Rev. B*, 2020, **101**, 134403.

35 F. Cugini, S. Chicco, F. Orlandi, G. Allodi, P. Bonfá, V. Vezzoni, O. N. Miroshkina, M. E. Gruner, L. Righi, S. Fabbri, F. Albertini, R. De Renzi and M. Solzi, *Phys. Rev. B*, 2022, **105**, 174434.

36 Y. Zhang, J. Bai, K.-L. Guo, J.-X. Xu, J.-L. Gu, N. Morley, Q.-Z. Gao, Y.-D. Zhang, C. Esling, X. Zhao and L. Zuo, *Rare Metals*, 2024, **43**, 1769–1785.

37 A. Kosogor, R. Y. Umetsu, V. Golub, X. Xu and R. Kainuma, *Journal of Alloys and Compounds*, 2024, **988**, 174130.

38 A. Çakır, M. Acet, U. Wiedwald, T. Krenke and M. Farle, *Acta Materialia*, 2017, **127**, 117–123.

39 T. Krenke, A. Çakır, F. Scheibel, M. Acet and M. Farle, *Journal of Applied Physics*, 2016, **120**, year.